Determination of combined measurement uncertainty via Monte Carlo analysis for the imaging spectrometer ROSIS

Karim Lenhard

Deutsches Zentrum für Luft- und Raumfahrt (DLR), Institut für Methodik der Fernerkundung (IMF), 82234 Oberpfaffenhofen, Germany (karim.lenhard@dlr.de)

Received 5 January 2012; revised 3 April 2012; accepted 13 April 2012; posted 13 April 2012 (Doc. ID 160949); published 13 June 2012

To enable traceability of imaging spectrometer data, the associated measurement uncertainties have to be provided reliably. Here a new tool for a Monte-Carlo-type measurement uncertainty propagation for the uncertainties that originate from the spectrometer itself is described. For this, an instrument model of the imaging spectrometer ROSIS is used. Combined uncertainties are then derived for radiometrically and spectrally calibrated data using a synthetic at-sensor radiance spectrum as input. By coupling this new software tool with an inverse modeling program, the measurement uncertainties are propagated for an exemplary water data product.

OCIS codes: 120.0280, 120.3940, 280.4788.

1. Introduction

The goal of this paper is to present the use of Monte Carlo analysis for the propagation of measurement uncertainties of radiometrically and spectrally calibrated imaging spectrometer data as well as their impact on retrieved model parameters of an exemplary application. The indication of measurement uncertainties for scientifically used data is necessary to allow for an estimation the uncertainty of subsequent analyses of the taken data and to enable comparability of data between different sensors. This method was implemented into a software tool called PyROSIS.

The need for the indication of measurement uncertainties has been recognized by the hyperspectral remote sensing community [1]. Therefore, traceability to the Systeme International units of the spectral radiance data recorded by imaging spectroradiometers is increasingly a requirement, e.g., [2].

According to metrological guidelines [3], propagation of measurement uncertainties should be performed numerically using a Monte Carlo method (MCM) if an analytical error propagation is not feasible. This is the case for imaging spectrometer data, since, for example, radiometric uncertainties introduced through spectral uncertainties cannot be determined analytically, as they depend on the object spectra [4]. Also, some data processing procedures performed to process raw data [Level 0 (L0) data] to radiometrically and spectrally calibrated data [Level 1 (L1) data] cannot be modeled for an analytical error propagation, such as geometric or spectral resampling or stray light correction.

Since the uncertainties depend on the instrument, this simulation is based on the implementation of a specific sensor. For this study, Deutsches Zentrum für Luft- und Raumfahrt's (DLR's) imaging spectrometer ROSIS was chosen, as laboratory and airborne characterization data were readily available. These data are used for the calibration as well as for the generation of the sensor model for the simulation. Also, the L1-calibration software, which needs to

1559-128X/12/184065-08$15.00/0

be included in the Monte Carlo simulation, was available.

The input spectra that are used to generate at-sensor radiances in this simulation are synthetic: a water reflectance spectrum was generated and propagated through the atmosphere to simulate at-sensor radiances across the field of view. The water reflectance was generated by the software WASI [5].

By coupling PyROSIS with WASI into one workflow, the L1 data that are generated in this simulation can be used to estimate the instrument's influence on the uncertainties of the retrieved parameters of the radiative transfer model. This is shown here exemplarily for the determination of suspended matter concentration by inverse modeling using WASI.

The focus of this paper is on radiometric and spectral uncertainties; uncertainties introduced via geometric properties such as finite line spread functions (i.e., imaging of multiple objects within one pixel) or movement smearing are not considered here. These are studied in more detail in, e.g., [6]. Hence, the simulated scene used for this study is chosen to be homogeneous. Also, the uncertainties introduced through atmospheric and geometric correction are not included in this analysis, as this also was studied previously, for instance in [1,7].

This paper is organized as follows. Section 2 gives a brief recapitulation of how Monte Carlo analyses are used to determine measurement uncertainties, Section 3 presents the implementation of such an analysis into software, and Section 4 introduces the instrument model used in this study. Results obtained with the Monte Carlo analysis are presented in Section 5 and commented on in Section 6.

2. Determination of Measurement Uncertainties via the MCM

To describe the measurement uncertainties, a probability density function (PDF) or a probability distribution is assigned to each sensor and model parameter (see Section 4). After that, an MCM analysis is performed as follows.

- Select the number N of hyperspectral frames to be simulated.
- For each run of the simulation, i.e., each frame, draw a random value from each parameter's PDF and perform a forward calculation with those values to simulate the data acquisition process, the calibration, and subsequent processing steps.
- Repeat this N times to build the PDFs of the at-sensor radiance.
- Determine the shortest 95% coverage intervals.

The shortest 95% coverage interval is the smallest interval that contains 95% of the radiance values of a detector element. Reference [3] recommends the use of shortest coverage intervals in case of potentially asymmetric and *a priori* unknown PDFs of the results. For a Gaussian PDF, this corresponds to a coverage factor of $k = 2$, meaning 2 standard deviations.

Each run of the simulation by PyROSIS consists of the following steps.

- Simulate the image acquisition process using the instrument model for a given remote sensing reflectance spectrum at a well-defined viewing and illumination geometry and atmospheric conditions. This corresponds to the creation of a synthetic hyperspectral frame, which includes all spectral information of one image line, i.e., all the information collected by the instrument during one sampling; the units of the data being digital numbers (DNs).
- Perform L0 to L1 calibration. The data are now in the units of spectral radiances.
- Correct for atmosphere and illumination. The data now have the units of normalized water leaving remote sensing reflectance.
- Further analysis of the reflectance data through inverse modeling using WASI.

The hyperspectral frame is defined here as one image row of the hyperspectral cube, i.e., one spectrum for each geometric pixel.

3. Implementation of the Method

A. Work Flow

The first step is to create a hyperspectral frame, i.e., one spectrum for each geometric pixel using a simulated at-sensor radiance spectrum. This corresponds to the imaging of a completely homogeneous scene during a flight.

The second step consists in the calibration of this frame, so that one ends up with radiance spectra.

The calibrated spectra are atmospherically corrected and finally handed over to WASI to retrieve the suspended matter concentration, C_L.

B. Generation of Synthetic Imaging Spectrometer Frame

In the following, the generation of an imaging spectrometer frame is described. Some of the processing steps are explained in more detail in Subsection 3.C.

First, an at-sensor radiance spectrum L is calculated as follows:

$$L(\lambda) = R_{\mathrm{RS}}(\lambda) \cdot T_{\mathrm{atm}}(\lambda) \cdot E_0(\lambda) \cdot T_{\mathrm{window}}(\lambda) + L_{\mathrm{path}}(\lambda). \tag{1}$$

In this equation, R_{RS} denotes the water remote sensing reflectance, T_{atm} an atmospheric transmission generated with MODTRAN [8], E_0 the extraterrestrial solar irradiance [9], T_{window} the transmission of the airplane window, and L_{path} the path radiance. All input spectra have a higher resolution ($\Delta\lambda \approx 1$ nm) than the simulated instrument (for ROSIS, $\Delta\lambda \approx 6$ nm). T_{atm} is the product of the atmospheric transmission of the downwelling irradiance reaching the surface $T_{\mathrm{atm}}^{\mathrm{down}}$ and the atmospheric transmission of the upwelling radiance between water surface and sensor $T_{\mathrm{atm}}^{\mathrm{up}}$.

In the following, S denotes a sensor signal in the units of DN. The index i denotes spectral channels, the index j denotes geometric pixels. For the sake of readability, some equations take the form of matrix equations, where variables that are subscripted with only one index are to be understood as a vector; i.e., S_j is a vector containing the spectral information recorded by the geometric pixel number j. Matrices are in bold typeface.

For each geometric pixel, the radiance impinging each channel is then calculated by integrating the product of the spectral response function (SRF) SRF(λ) with the at-sensor radiance spectrum, thus yielding a radiance spectrum L_{LR} with lower resolution:

$$L_{\mathrm{LR},i,j} = \int \mathrm{SRF}(\lambda)_{i,j} \cdot L(\lambda) \mathrm{d}\lambda. \tag{2}$$

The center wavelengths of the detector element's SRF are calculated according to Section 4. An error due to polarization sensitivity is introduced multiplicatively:

$$L_{\mathrm{LR,Pol},i,j} = L_{\mathrm{LR},i,j}(1 + P \cdot U(\phi, i)), \tag{3}$$

$P = 30\%$ being a typical degree of polarization due to the reflection on water and U being the probability distribution described in Eq. (14).

Subsequently, the photoresponse nonuniformity (PRNU) is introduced. This is done by multiplying the signal of each detector element with the inverse of its PRNU correction factor, U_{PRNU}.

Then, the radiances are converted into DN:

$$S_{i,j} = L_{\mathrm{LR,Pol},i,j} \cdot r_{i,j} \cdot t_{\mathrm{exposure}}, \tag{4}$$

where the radiometric response coefficients are computed according to the following equation:

$$r_j = \frac{1}{L_{\mathrm{IS}} \cdot t_{\mathrm{exposure}}} \cdot \boldsymbol{M} \cdot \left(\frac{S_{\mathrm{IS},j}}{U_{\mathrm{PRNU},j}} - S_{\mathrm{smear},j} \right). \tag{5}$$

The radiometric response coefficients $r_{i,j}$ depend on wavelength and pixel number. S_{IS} is the signal measured by the sensor of an integrating sphere, L_{IS} is the spectral radiance of that sphere, and t_{exposure} is the exposure time. The signal is corrected for PRNU (U_{PRNU}), smear (S_{smear}), stray light using the current stray light distribution, $\boldsymbol{M}$, and smile via resampling to the reference wavelengths. A stray light distribution matrix $\boldsymbol{M}$ is generated for each run using Eq. (11).

The effects taken into account for the calculation of r have to be applied to S as well to simulate L0 data: spectral stray light is added by multiplying each pixels' spectrum with the inverse of the correction matrix. Readout smearing is added using Eq. (15). The dark current signal as well as its associated uncertainty are then added to the signal. The radiometric noise is generated using Eq. (12) and added. Detector saturation is introduced by setting signals above the detectors' maximal signal level to its maximal signal level. Finally, quantization errors are introduced to the data by rounding the signals to the next integer number. A more detailed description of these effects is given in Section 4.

C. L1 Calibration

The L1 calibration for synthetic data uses the same procedure as the regular L1 calibration process, the difference being that calibration errors are added here. The calibration steps performed are, in the same order as presented here, starting with the signals S generated according to Subsection 3.B:

The dark current is subtracted. Then, the PRNU is corrected by multiplying the signal of each detector element with its individual PRNU correction factor. The signal due to smearing is corrected for by calculating it with Eq. (15) and subtracting it from the signal. The stray light signals are removed according to Section 4. To correct for the spectral misregistration due to smile, all spectra are resampled to a single, defined set of center wavelengths using cubic spline interpolation. Finally, the resulting signal of each detector element $S'_{i,j}$ is multiplied with the detector element's radiometric response

$$L_{i,j} = \frac{S'_{i,j}}{r_{i,j} \cdot t_{\mathrm{exposure}}}, \tag{6}$$

so that the data are now radiometrically calibrated and in the units of spectral radiance.

D. Level 2 Processing

To allow further analyses, the L1 calibrated data have to be processed to Level 2; i.e., the spectral radiance has to be atmospherically corrected so that the at-sensor radiances are converted into ground reflectances. As the atmospheric contribution is completely known in these simulations, this is an idealized correction. This is done via

$$R_{\mathrm{RS}} = \frac{L(\lambda) - L_{\mathrm{path,LR}}(\lambda)}{E_{0,\mathrm{LR}}(\lambda) \cdot T_{\mathrm{atm,LR}}(\lambda) \cdot T_{\mathrm{window,LR}}(\lambda)}, \tag{7}$$

where the denominator, the combined spectrum of the Sun, the atmosphere, and the aircraft window transmission as well as the path radiance are resampled to the lower resolution of ROSIS, as indicated by the subscript "LR."

E. Generation of Level 3 Data

The "Water Colour Simulator" WASI [5] is a software tool that, in its forward mode, is capable of the calculation of optical water spectra based on physical models. In its inverse mode, WASI allows for the inversion of water spectra for the retrieval of water model parameters.

WASI was used in its forward more to generate the remote sensing reflectance spectrum used for the

simulation. Therefore, all input parameters for the generation of this spectrum are known. For this study, only the suspended matter concentration C_L was retrieved. Since this is done for each simulated spectrum of each simulated sensor frame, a combined measurement uncertainty can be determined for the retrieval of C_L by again using the shortest 95% coverage interval for all the resulting values of C_L as a measure for the uncertainty.

F. Software Tool PyROSIS

The L1 calibration software and the Monte Carlo simulation tool were implemented in Python, using the NumPy and SciPy libraries.

The sensor model description is based on text files, so the implementation of other instruments should be relatively simple. On an Intel i5 notebook processor with 2.67 GHz, the calculation of a single frame on one core takes about 30 s. Since the task is easily parallelized, the software can make use of multiple processor cores.

4. ROSIS Sensor Model

The term "sensor model" is used here in the sense that it is a mathematical description of an imaging spectrometer. All values given here are derived from the available, although partly unpublished, data and are based on laboratory and airborne measurements. As the scope of this publication does not encompass the actual characterization of ROSIS, the derivation of those values is not described here in more detail.

ROSIS [10,11] is a grating-based imaging spectrometer that has been used in three different configurations since 1991. The current configuration, ROSIS 3, has 512 geometric pixels, 115 spectral channels, 103 of which are usable for airborne measurements, and a radiometric resolution of 14 bits. The remaining 12 channels are blocked by an optical filter. ROSIS covers the wavelength range from 430 to 836 nm. Table 1 provides an overview of the sensor parameters and their uncertainties, which are used to model the measurement uncertainties of ROSIS.

Table 1. ROSIS Sensor Parameters Used for MCM with Their Associated Uncertainties[a]

Parameter	Mean Value	Uncertainty	PDF
Center wavelength	see Eq. 8	0.2 nm	Gaussian
FWHM of SRF	6 nm	0.1 nm	Gaussian
Spectral sampling interval	4 nm	0.01 nm	Gaussian
Radiometric response	From table	1%	Gaussian
Aircraft window transmission	From table	1.5%	Uniform
Polarization sensitivity	see Eq. 13	see Eq. 14	Arc sine
Dark current	900 DN	0.6 DN	Gaussian
Spectral stray light	see Eq. 11	5%	Gaussian
PRNU	From table	0.5%	Gaussian
Radiometric noise	0	see Eq. 12	Gaussian

[a]Gaussian uncertainties are given for $k = 1$. Some parameters and uncertainties are defined through the referenced equations. "From table" refers to the look-up tables in which the measurement data are stored.

The following are parameters of the sensor model.

SRFs. The SRF of a ROSIS channel is Gaussian in shape, with a FWHM of $\lambda_{\mathrm{FWHM}} = 6$ nm and an uncertainty of $\Delta\lambda_{\mathrm{FWHM}} = 0.1$ nm. The spectral sampling interval (SSI) between two adjacent channels is $\lambda_{\mathrm{SSI}} = 4$ nm, with an uncertainty of $\Delta\lambda_{\mathrm{SSI}} = 0.01$ nm. The central wavelength $\lambda_{c,i}$ of a channel i has a stability of $\Delta\lambda_c = 0.2$ nm during a flight strip. All three uncertainties are modeled with Gaussian PDFs.

The spectral smile effect is also taken into account by introducing a pixel-number-dependent spectral shift to all λ_c of each geometric pixel. The introduced shifts are up to 1.5 nm and follow a parabolic function. The uncertainty of the smile shift is set to be zero, since the smile can be accurately measured in the laboratory and the remaining uncertainty corresponds to the uncertainty in center wavelength position.

The center wavelengths are computed as follows:

$$\lambda_{c,i,j} = 380\ \mathrm{nm} + \lambda_{\mathrm{SSI}} \cdot i - \lambda_{\mathrm{smile},j}, \tag{8}$$

with the smile shift relative to pixel $j = 0$ being parametrized as

$$\lambda_{\mathrm{smile},j} = (-9.52 \cdot 10^{-6} j^2 + 6.48 \cdot 10^{-3} j)\ \mathrm{nm}. \tag{9}$$

Spectral stray light. Spectral stray light can be understood as optical cross talk: Detector elements "see" light of wavelengths that should impinge on other spectral channels. A spectral stray light correction algorithm is described in [12], and the corresponding measurements are described in [13]. The stray light distribution can be condensed into a matrix $\boldsymbol{M}$, such that the equation

$$S_{\mathrm{meas},j} = \boldsymbol{M} \cdot S_{\mathrm{in},j} \tag{10}$$

holds. S_{in} is a vector with the spectrum that would be recorded without stray light influence, while the vector S_{meas} is the spectrum actually recorded by the pixel j of the instrument. The same matrix is applied to all geometric pixels. This approach only accounts for stray light that has its origin in the covered wavelength interval; stray light that originates from outside this interval is neglected.

The stray light matrix is generated from a parametrization of the stray light in ROSIS:

$$\boldsymbol{M}_{k,k_0} = \frac{a}{b(k-k_0)^2+1} + \frac{c}{d(k-k_0)^4+1} + h, \tag{11}$$

with $a = 8.43 \cdot 10^{-4}$, $b = 9.83 \cdot 10^{-4}$, $c = -2.56 \cdot 10^{-4}$, $d = -5.58 \cdot 10^{-4}$, and $h = 7.56 \cdot 10^{-5}$. k denotes the channel that receives stray light from the channel k_0. The PDF for each parameter is chosen to be Gaussian in shape, with a width of 5%.

Radiometric response. ROSIS' calibration standard is an integrating sphere calibrated at the German National Metrology Institute (PTB). In the

relevant part of the spectrum, the sphere's emitted spectral radiance uncertainty is given as $\sigma_L = 1\%$, with a Gaussian PDF. No radiometric nonlinearities were introduced as these can be neglected for the studied sensor.

PRNU. PRNU measurements were made before the focal plane array was built into the instrument with a homogeneous light source. The uncertainty is $\sigma_{\mathrm{PRNU}} = 0.5\%$, with a Gaussian PDF. For both PRNU correction and radiometric calibration, the actual radiometric reference files are used here.

Mean dark current level. The mean dark current level has an uncertainty of $\sigma_{\mathrm{D.C.}} = 0.6$ DN during a flight strip and follows a Gaussian distribution. For the simulation, a dark current signal level of 900 DN is used. The uncertainty $\sigma_{\mathrm{D.C.}}$ is added as a constant offset to all detector elements.

Radiometric noise. The radiometric noise of the instrument has a Gaussian PDF, its width σ_{noise} given by the functional relationship

$$\sigma_{\mathrm{noise}} = (12.38 + 0.001743 \cdot S)\ \mathrm{DN}, \tag{12}$$

which is a parametrization of the noise levels measured in ROSIS. All noise sources, i.e., dark current noise, noise from the readout electronics, and photon noise, are included here. Unlike $\sigma_{\mathrm{D.C.}}$, the noise function is applied to all pixels individually.

Aircraft window transmission. Transmission measurements were performed with two laboratory spectrophotometers. A comparison of the results of the two spectrophotometers yields a wavelength-independent measurement uncertainty with a uniform PDF with a width of 1.5%.

Polarization sensitivity. The sensitivity to linear polarization is modeled to increase linearly from 5% at shorter wavelengths to 15% at longer wavelengths over the spectral range of the instrument; i.e., the polarization sensitivity p_i of a channel i is given by

$$p_i = 8.7 \cdot 10^{-4} i + 0.05. \tag{13}$$

The distribution function

$$U(\phi, i) = \frac{p_i}{2} + \frac{p_i}{2}\ \sin(\phi) \tag{14}$$

is used to model the uncertainty of the polarization of the incident light. According to [3], this is the probability distribution for sinusoidally varying quantities with an unknown phase ϕ.

Readout smearing. ROSIS does not have a shutter, and the readout of the CCD detector array is done in the frame transfer mode. Thus, the smear signal $S_{\mathrm{smear},j}$ of each pixel j is calculated with the following equation:

$$S_{\mathrm{smear},j} = \sum_{i=1}^{115} S_{i,j} \cdot \frac{t_{\mathrm{smear}}}{t_{\mathrm{exposure}}}, \tag{15}$$

with $t_{\mathrm{smear}} = 1.8 \cdot 10^{-6}$ s as the readout time and $t_{\mathrm{exposure}} = 1/40$ s as the exposure time.

Note that, except for the radiometric noise, the uncertainties are introduced so that no additional noise is generated; e.g., the entire radiometric response array is varied scalarly within the values given in Table 1, meaning that the radiometric calibration array used in a run of the MCM $\boldsymbol{r}$ is the product of the reference radiometric calibration array $\boldsymbol{r}_{\mathrm{ref}}$ and a random scalar z.

5. Results

PyROSIS can be used to calculate traceable measurement uncertainties for radiometrically calibrated data and their derived data products as well as to perform sensitivity analyses to relate the uncertainties of sensor parameters to the uncertainties in the product of interest. Examples for this are presented in this section.

A. Number of Runs

The number of runs to be repeated to get an accurate estimate of the uncertainty has to be determined. For Fig. 1, 1000 frames were calculated, and the standard deviation for the signal level of the detector at pixel 300, channel 90 was computed using an increasing number of frames. The standard deviation settles quickly to a value of about 0.53 mW/($\mathrm{m}^2 \cdot \mathrm{sr} \cdot \mathrm{nm}$), with variations not larger than 3% of that value. For the reason of economy of time, a lower number of frames, 200, is generated for the plots in the following sections. Because of the long computation times, the total number of runs is well below the required number to build a good approximation of the output PDF but is still in accordance with [3], as this approach allows for a uncertainty estimation in finite time and this accuracy is sufficient for the presentation of this method.

B. Tests of the Sensor Simulation

A test case for the sensor simulation is shown in Fig. 2: a laboratory L0 spectrum, generated by

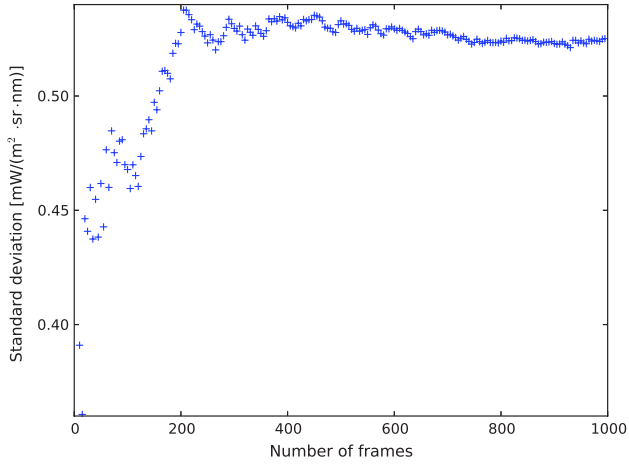

Fig. 1. (Color online) Standard deviation of the signal of one detector element depending on how many Monte Carlo frames are used.

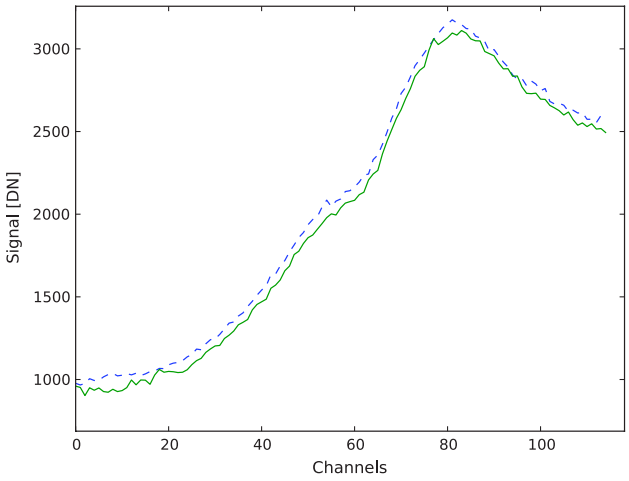

Fig. 2. (Color online) Comparison of two L0 spectra—one simulated from the calibration data and our integrating sphere (solid line) and one from a laboratory measurement of the same sphere (dashed line).

illuminating the instrument with an integrating sphere, is compared to an L0 spectrum simulated with PyROSIS using the sphere's radiance spectrum. The differences between both spectra can be attributed to the difference in mean dark current level, noise, and change in the radiance of the sphere between the measurement of the spectrum used for simulation and the actual measurement of the sphere with ROSIS.

A second test is illustrated with Fig. 3: the reflectance input spectrum is compared to the reflectance obtained after simulation. As expected, the spectrum generated by the full simulation differs mostly by the noise contribution.

C. Traceable Measurement Uncertainties on Radiance Data

A major purpose of the software is to calculate measurement uncertainties for given spectra. An example is shown in Figs. 4 and 5. The continuous curve in

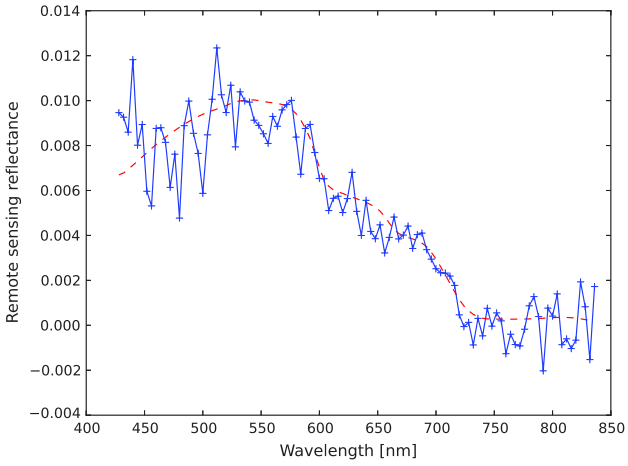

Fig. 3. (Color online) Comparison between the input reflectance spectrum generated by WASI (dashed line) and a retrieved spectrum calculated with all error sources (+ symbols).

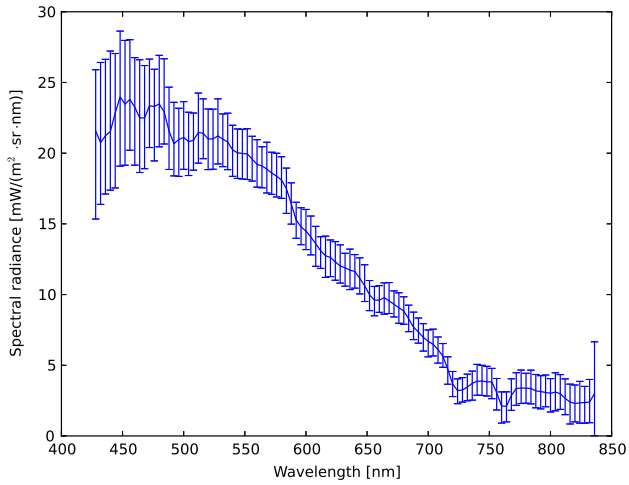

Fig. 4. (Color online) Mean calibrated spectrum with error bars defined through 95% coverage interval ($k = 2$).

Fig. 5 shows half of the error bars width shown in Fig. 4 divided by the actual value, corresponding to a relative uncertainty for $k = 2$.

For the given radiance levels, as shown in Fig. 5, the combined uncertainty is between 10% and 120% for $k = 2$. This is much larger than the radiometric calibration uncertainty of 2% that was set for the simulation. The increase of the measurement uncertainties for wavelengths smaller than 500 nm depicted in Fig. 5 is concordant with experience with ROSIS and can be explained with a low sensitivity of the instrument and the low radiance levels of the calibration source in that wavelength range. The increase of the combined uncertainty above 700 nm can be explained by the very low reflectance of water and the low level of path radiance.

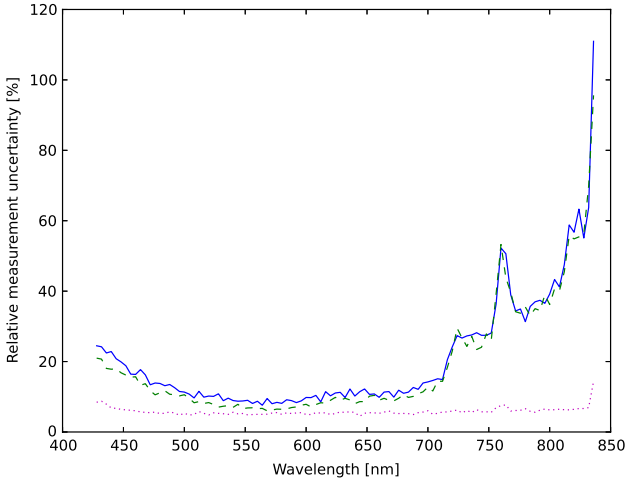

Fig. 5. (Color online) Combined measurement uncertainty for $k = 2$ for the spectral radiance data. The solid curve describes the uncertainties given all effects, the dashed curve the uncertainty obtained if only noise is an uncertainty source in the simulation, and the dotted curve the contributions of all other effects together.

D. Influence of Instrument Parameters

Further results are visible in Fig. 5, which shows the combined uncertainty for three different cases: all contributing effects are accounted for, all effects except the radiometric noise are considered, and only radiometric noise contributing to the uncertainty.

Figure 5 clearly illustrates that, for this kind of target, i.e., a water surface of low reflectance, particularly at wavelengths above 700 nm, radiometric noise is the dominating source of measurement uncertainty. Therefore, a more detailed breakdown of the uncertainty contributions of the other sensor model parameters was not studied further, as reduced calibration uncertainties would not improve the overall data quality.

E. End-to-End Simulation with PyROSIS and WASI

1. *Retrieval of C_L*

The simulated signal and uncertainties using PyROSIS can be used for the study of the measurement uncertainties of products derived from sensor data. After converting the simulated radiances into reflectances as described in Subsection 3.D, the simulated results from PyROSIS are used to calculate the uncertainties of a product, the suspended matter concentration C_L. This was done by performing a retrieval of C_L with WASI for a specific geometric pixel of each frame generated in the Monte Carlo simulation.

Figure 6 shows the relative uncertainties for the three described uncertainty models for the simulated reflectances obtained after the removal of atmospheric contributions to the spectra. The combined uncertainty of the data is of the order of 40% to 100% ($k = 2$). Again, the combined uncertainty is dominated by the noise contribution.

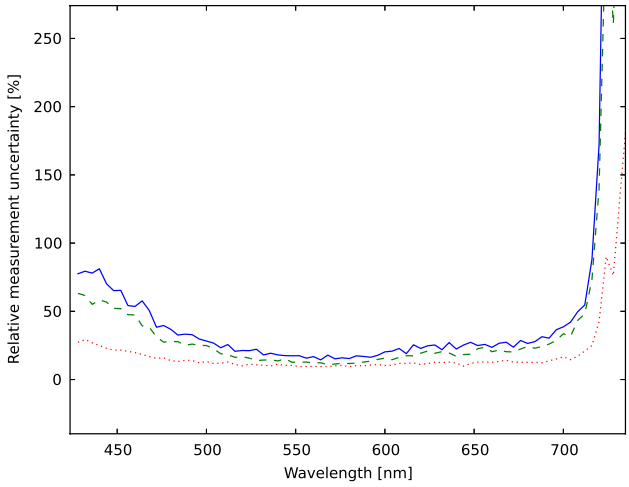

Fig. 6. (Color online) Combined measurement uncertainty for $k = 2$ for the remote sensing reflectance data. The solid curve describes the uncertainties given all effects, the dashed curve the uncertainty obtained if only noise is an uncertainty source in the simulation, and the dotted curve the contributions of all other effects together. The relative uncertainties for wavelengths greater 700 nm are not a reliable measure as the remote sensing reflectance is almost zero in all analyzed spectra.

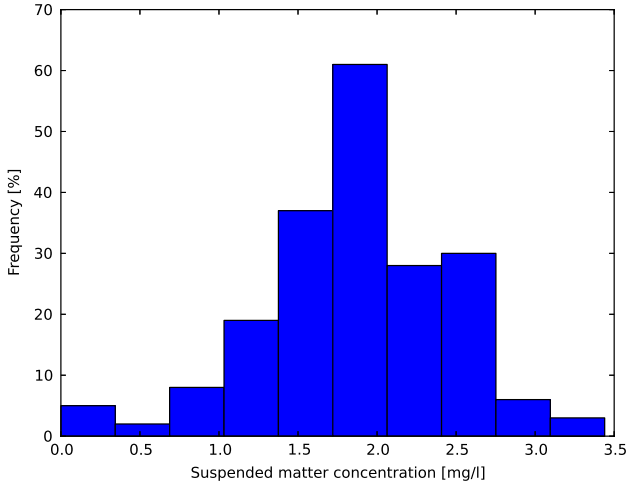

Fig. 7. (Color online) Histogram of the retrieved suspended matter concentrations. Actual concentration, $C_L = 2$ mg/l

The resulting distribution of C_L, derived from a pixel near the center of the detector array, is shown in the histogram in Fig. 7. The retrieved concentration of $C_L = 1.8 \pm 1.2$ ($k = 2$) shows the large influence of the sensor uncertainties on the retrieval.

2. *Influence of Stray Light Correction of C_L Retrieval*

PyROSIS can be used to quantify the effect of each specific calibration step. For example, to estimate the influence of stray light on the retrieval of C_L, a PyROSIS simulation was performed in which the systematic error due to stray light was left uncorrected in the L1 calibration. As shown in Fig. 8, this leads to wavelength-dependent errors with maximum underestimation of radiance levels of 30%.

These differences in radiance levels lead to a complete failure of the retrieval: WASI estimates the suspended matter content to exactly zero in all cases.

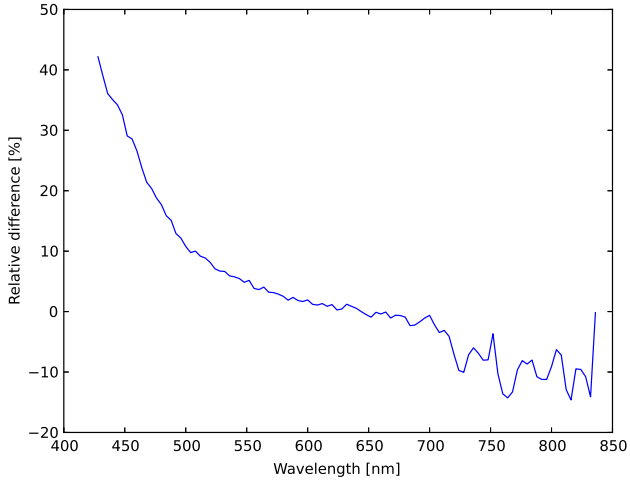

Fig. 8. (Color online) Relative difference between the averaged simulated radiance spectra with and without stray light correction.

6. Discussion

With PyROSIS, to the authors best knowledge, it is for the first time possible to compute the traceable measurement uncertainties for L1 data of hyperspectral sensors, and these kinds of analyses are required if remote sensing data products are to obtain credible measurement uncertainties.

Another feature of PyROSIS that was demonstrated is the assessment of the contribution of the individual uncertainties of the sensor properties to the combined uncertainty. This is needed to assess the improvement achievable through laboratory characterization. The conclusion of Subsection 5.D is that, due to the radiometric noise dominance, improved laboratory characterization procedures for other sensor parameters cannot improve the data quality. Instead, it motivates us to analyze the reduction of radiometric noise, which can be achieved through software or hardware binning of the data.

PyROSIS was used in conjunction with WASI to perform a complete end-to-end simulation to obtain combined measurement uncertainties for an end product based on sensor parameters. The example used in this study was the suspended matter concentration C_L. Possible next steps include the derivation of combined uncertainties for a more realistic multiparameter retrieval or derivation in combination with an atmospheric correction.

Finally, with PyROSIS, more realistic simulated spectra can be generated. This can assist the retrieval algorithm development if the algorithms can be designed considering sensor specific systematic effects. Also, the sensitivity of algorithms to sensor measurement uncertainties can be assessed this way.

7. Conclusion

In this paper, software capable of using imaging spectrometer characterization data to propagate measurement uncertainties through different product levels with a Monte Carlo approach has been presented. This is necessary to calibrate hyperspectral data in a traceable way and to expand previous studies concerning error propagation and estimation of hyperspectral data, such as [1,6,14]. While scene simulators are a prerequisite for algorithm development [15], this type of analysis is necessary for estimating the influence of sensor performance on data products, helpful for sensor optimization, and could assist algorithm development.

It is planned to expand this software to incorporate more instruments when characterization data of these sensors become available. Finally, this tool will be used to define scientifically motivated requirements for DLR's calibration laboratory and to identify limiting measurement procedures and equipment.

The author would like to thank Peter Gege and the anonymous reviewer for their valuable comments.

References

1. J. Beekhuizen, M. Bachmann, E. Ben-Dor, J. Biesemans, M. Grant, G. Heuvelink, A. Hueni, M. Kneubuehler, E. de Miguel Llanes, A. Pimstein, E. Prado Ortega, I. Reusen, T. Ruhtz, and M. Schaale, "Report on full error propagation concept," DJ2.1.2, EUFAR FP7 JRA2—HYQUAPRO (European Facility For Airborne Research, 2009).
2. H. Kaufmann, K. Segl, S. Chabrillat, S. Hofer, T. Stuffler, A. Mueller, R. Richter, G. Schreier, R. Haydn, and H. Bach, "EnMAP a hyperspectral sensor for environmental mapping and analysis," in *Proceedings of the IEEE International Conference on Geoscience and Remote Sensing Symposium, 2006* (IEEE, 2006), pp. 1617–1619.
3. Joint Comittee for Guides in Metrology, "JCGM 101: 2008, Evaluation of measurement data—Supplement 1 to the 'Guide to the expression of uncertainty in measurement'—Propagation of distributions using a Monte Carlo method," Tech. Rep. (Bureau International des Poids et Mesures, 2008).
4. R. O. Green, "Spectral calibration requirement for Earth-looking imaging spectrometers in the solar-reflected spectrum," Appl. Opt. **37**, 683–690 (1998).
5. P. Gege, "The water colour simulator WASI: an integrating software tool for analysis and simulation of optical *in situ* spectra," Comput. Geosci. **30**, 523–532 (2004).
6. P. Schwind, R. Müller, G. Palubinskas, T. Storch, and C. Makasy, "A geometric simulator for the hyperspectral mission EnMAP," presented at the Canadian Geomatics Conference, Calgary, Alberta, Canada, 15–18 June 2010.
7. R. Richter and D. Schläpfer, "Geo-atmospheric processing of airborne imaging spectrometry data. Part 2: atmospheric/topographic correction," Int. J. Remote Sens. **23**, 2631–2649 (2002).
8. A. Berk, L. S. Bernstein, and D. C. Robertson, "MODTRAN: a moderate resolution model for LOWTRAN 7," Tech. Rep. (Geophysics Laboratory, Air Force Command, U. S. Air Force, Hanscom Air Force Base, Massachusetts, USA, 1989).
9. H. Neckel and D. Labs, "The solar radiation between 3300 and 12500 Å," Sol. Phys. **90**, 205–258 (1984).
10. P. Gege, D. Beran, W. Mooshuber, J. Schulz, and H. van der Piepen, "System analysis and performance of the new version of the imaging spectrometer ROSIS," in *Proceedings of the 1st EARSeL Workshop on Imaging Spectroscopy* (European Association of Remote Sensing Laboratories, 1998), pp. 29–35.
11. J. Schulz, "Systemtechnische Untersuchungen an dem abbildenden Spektrometer ROSIS-01 zur Erfassung und Interpretation der Meeresfarbe," Ph.D. thesis (DLR Institut für Optoelektronik, 1997).
12. Y. Zong, S. W. Brown, B. C. Johnson, K. R. Lykke, and Y. Ohno, "Simple spectral stray light correction method for array spectroradiometers," Appl. Opt. **45**, 1111–1119 (2006).
13. K. Lenhard, P. Gege, and M. Damm, "Implementation of algorithmic correction of stray light in a pushbroom hyperspectral sensor," presented at the 6th EARSeL Workshop on Imaging Spectroscopy, Tel Aviv, 16–19 March 2009.
14. S. Lavender, O. F. D'Andon, S. Kay, L. Bourg, S. Emsley, N. Gilles, T. Nightingale, R. Quast, M. Bates, T. Storm, J. Hedley, M. Knul, G. Sotis, R. Nasir-Habeeb, and P. Goryl, "Applying uncertainties to ocean colour data," Metrologia **49**, S17–S20 (2012).
15. A. Börner, L. Wiest, P. Keller, R. Reulke, R. Richter, and M. Schaepman, "SENSOR: a tool for the simulation of hyperspectral remote sensing systems," ISPRS J. Photogramm. Remote Sens. **55**, 299–312 (2001).